metals

Article

Microstructure and Mechanical Properties of Novel Heat Resistant Cast Al-Cu-Yb(Gd)-Mg-Mn-Zr Alloys

Olga I. Mamzurina [1], Sayed M. Amer [2], Maria V. Glavatskikh [1], Ruslan Yu. Barkov [1], Irina S. Loginova [1] and Andrey V. Pozdniakov [1,*]

[1] Department of Physical Metallurgy of Non-Ferrous Metals, National University of Science and Technology "MISiS", Moscow 119049, Russia
[2] Faculty of Engineering, Mining, Metallurgy and Petroleum Engineering, Al-Azhar University, Cairo 11884, Egypt
* Correspondence: pozdniakov@misis.ru

Abstract: The present study focused on the development of the novel heat resistant cast Al-Cu-Yb(Gd)-Mg-Mn-Zr alloys based on the prevue investigations. Microstructures and mechanical properties were investigated by optical, scanning and transmission electron microscopy, hardness measurements, and tensile and creep tests at room and elevated temperatures. Ytterbium in combination with Zr and Ti provide greater Al grain refining than gadolinium. The $L1_2$-$Al_3(Zr,Yb)$ or $L1_2$-$Al_3(Zr,Gd)$ and $Al_{20}Cu_2Mn_3$ phase precipitates were nucleated during solution treatment. The average sizes of $L1_2$-$Al_3(Zr,Yb)$ and $L1_2$-$Al_3(Zr,Gd)$ are 28 ± 6 nm and 32 ± 4 nm, respectively. $Al_{20}Cu_2Mn_3$ phase precipitates formed with a more coarse size of 100–200 nm. The highest hardening effect was achieved after 3 h of aging at 210 °C in both alloys due to S′(Al_2CuMg) precipitates. The ultimate tensile strengths (UTS) of the AlCuYbMg and AlCuGdMg alloys at room temperature are 338 and 299 MPa, respectively. The UTS decreases to 220–272 MPa when increasing the temperature of the tensile test to 200–250 °C. The rupture stress at 250 °C for 100 h under stress is 111–113 MPa. The contribution from different structure parts in the yield strength was calculated. The main strengthening effects of 54–60 MPa and 138–153 MPa were achieved from $L1_2$ and S′ precipitates, respectively. The calculated values of yield strength (YS) are consistent with the experimental data. Novel AlCuYbMg and AlCuGdMg alloys are a potential option for castings for high temperature application.

Keywords: cast aluminum alloys; microstructure; mechanical properties; precipitates; heat resistance

check for updates

Citation: Mamzurina, O.I.; Amer, S.M.; Glavatskikh, M.V.; Barkov, R.Y.; Loginova, I.S.; Pozdniakov, A.V. Microstructure and Mechanical Properties of Novel Heat Resistant Cast Al-Cu-Yb(Gd)-Mg-Mn-Zr Alloys. *Metals* **2022**, *12*, 2079. https://doi.org/10.3390/met12122079

Academic Editors: Angelo Fernando Padilha and Nikki Stanford

Received: 8 November 2022
Accepted: 1 December 2022
Published: 3 December 2022

1. Introduction

Aluminum alloys are the most popular lightweight materials for the automobile and aerospace industries due to their good combination of strength at room and elevated temperatures, density, casting properties and corrosion resistance [1,2]. Al-Cu-based cast alloys demonstrate a high strength and heat resistance but the worst casting properties, for example, high sensitivity for hot tearing [2–5].

There are several ways to improve the casting properties of Al-Cu-based alloys. Additional alloying by eutectic forming elements, such as Fe, Ni, Si, and Mn, provides an improvement in the hot tearing sensitivity, but the strengthening effect is lower [2,4,5]. Doping by trace amounts of rare earth metals (REM) as grain refiners, for example, yttrium, is a good way to improve the hot tearing resistance [6]. The most common way is to search the novel base systems to develop high technology Al alloys.

Recent studies have demonstrated a perspective of the ternary quasibinary system Al-Cu-REM, where REM = Ce, Y, Er, Yb and Gd, due to a narrow solidification range and high thermal stability of the intermetallic phases [7–17]. The mechanical properties of the ternary alloy can be effectively improved by Zr [18–21] and Mn [22–24] additions, which provide precipitation strengthening. Sequential alloying led to the development of novel heat resistant casting and wrought alloys based on the Al-Cu-Y and Al-Cu-Er systems [25,26]. Novel alloys strengthen the eutectic phase particles, and $L1_2$-Al_3(Zr,REM) and $Al_{20}Cu_2Mn_3$ phase precipitates formed during solution treatment, and the S′ (Al_2CuMg) phase of the aging origin [18–26].

In addition, small additives of Yb or Gd may improve the mechanical properties and corrosion resistance of the Al-Cu-Mg and Al-Zn-Mg-Cu alloys [27–32]. For example, Yb refines the grains, decreases the precipitation temperature of Ω phase, accelerates the aging hardening process, and increases the maximum hardness and the tensile strength of the extruded Al-Cu-Mg-Ag [22]. Ytterbium and gadolinium with zirconium provide an increase in the room and high temperature mechanical properties of the Al-Si-Mg alloys [33–35]. The main strengthening mechanism in the Yb- or Gd-containing alloys with Zr is $L1_2$-Al_3(Zr,REM), which precipitates nucleation [36–39]. The same strengthening effect should be achieved with scandium alloying but scandium is very expansive [40].

The present study focused on the development of the novel heat resistant cast Al-Cu-Yb(Gd)-Mg-Mn-Zr alloys based on the prevue investigations [17,21,24]. The microstructure evaluation during casting and heat treatment, which provide excellent mechanical properties at room and elevated temperatures, will be presented.

2. Materials and Methods

Alloys with compositions presented in Table 1 were melted in the resistance furnace from pure Al (99.7%) and Mg (99.9%), and Al-10Yb, Al-10Gd, Al-10Mn, Al-5Zr, Al-5Ti-1B master alloys. Melting and pouring temperature was in the range of 780–800 °C. The master alloys with Mn, Zr, and Yb or Gd were successively introduced into the Al melt at 800 °C. Then pure Mg was introduced into the melt using titanium "bell". Al-5Ti-1B master alloy as a grain refiner was introduced in the melt before casting. Casting was carried out in the steel and copper water-cooling molds with cooling rate about 10–15 °C/s. The hot tearing index (HCI) was determined using "pencil" probe [2–5]. The average value of the HCI was calculated from three pourings.

Table 1. Chemical composition (wt.%) of the investigated alloys.

Alloy	Al	Cu	Yb or Gd	Mg	Mn	Zr	Fe	Si	Ti
AlCuYbMg	bal.	4.1	2.0	1	0.8	0.3	0.15	0.15	0.15
AlCuGdMg	bal.	4.5	2.7	1.1	0.8	0.3	0.15	0.15	0.15

Microstructure was investigated in detail with optical microscope (OM) Zeiss, scanning electron microscope (SEM) TESCAN VEGA 3LMH (Tescan, Brno, Czech Republic) and transmission electron microscope (TEM) JEOL–2100 EX (Jeol Ltd., Tokyo, Japan). Phase analysis was performed using X-ray diffraction (XRD) with Cu-Kα radiation on a Bruker D8 Advance diffractometer. Chemical composition of the alloys was determined by SEM electron diffraction X-ray (EDX) analyses. The grain structure of as-cast samples was investigated using OM under polarized light. The microstructure was revealed by anodizing (15–25 V, 0–5 °C) using Barker's reagent (46 mL of HBF_4, 7 g of HBO_3 and 970 mL of H_2O). The average value of the grain size was measured by random secant method in 3 images. The specimens for TEM were prepared using the A2 electrolyte on Struers Tenupol-5 equipment. The solidus temperatures were determined by the Labsys Setaram differential scanning calorimeter (SETARAM Instrumentation, Caluire, France) (DSC). Ingots were solution treated at 555–565 °C for 3 h in the Nabertherm furnace. Aging treatment was carried out at 150, 180 and 210 °C in in the SNOL furnace. The hardness was measured by the standard Vickers method under 5 kg load. The hardness value HV was determined as the arithmetic mean of five measurements and the standard deviation was calculated. The tensile samples with diameter of 5 mm and gage length of 25 mm were stretched on a Zwick/Roell Z250 Allround (Zwick/Roell, Kennesaw, GA, USA) test machine. Three samples were tested per condition. The rupture stress at 250 °C for 100 h under stress was determined on the Instron M3 test machine.

3. Results and Discussion

Zirconium and titanium elements are well known grain refiners in the Al alloys. The effect of grain refining should be increased in combination with other REM. For example, Er significantly refines the grain structure due to an increase in the nucleation centers [25,41–43]. The as-cast grain structures of the investigated alloys are presented in Figure 1. Ytterbium (Figure 1b) in combination with Zr and Ti provides greater refining than gadolinium (Figure 1a). The average grain sizes of the AlCuYbMg and AlCuGdMg alloys are 60 ± 12 and 100 ± 15 µm, respectively.

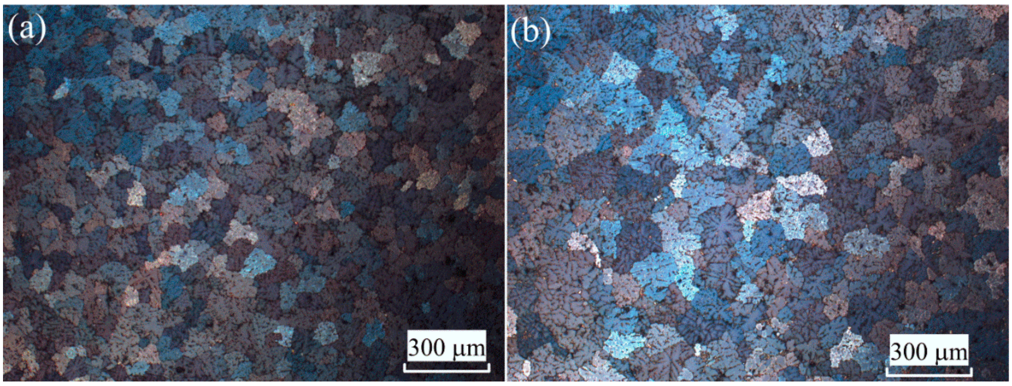

Figure 1. As-cast grain structures of the (**a**) AlCuYbMg and (**b**) AlCuGdMg alloys (OM).

Prevue's study was targeted at the structures and properties of the same alloys without Mg, Fe and Si impurities [19]. $Al_{80\text{-}88}Cu_{8\text{-}12}Yb_{3\text{-}4}Mn$ and $Al_{78\text{-}86}Cu_{10\text{-}15}Gd_{3\text{-}5}Mn$ phases of the solidification origin forms in the AlCuYbZrMn and AlCuGdZrMn alloys [24]. The same Mn-rich phases formed the eutectic microstructure in the investigated AlCuYbMg (Figure 2a,c) and AlCuGdMg (Figure 2b,d) alloys. In addition, Mn-rich phase particles with about 10% Mn were identified in the AlCuYbMg alloy. The formula of this phase can be written as $Al_{22}Cu_3Mn_2Yb$. Similar $Al_{25}Cu_4Mn_2Y$ [22] and $Al_{25}Cu_4Mn_2Er$ [23] phases were identified in the microstructures of the AlCuYZrMn and AlCuErZrMn alloys. Silicon impurity led to the $Al_{80}Yb_5Cu_6Si_8$ and $Al_{80}Gd_5Cu_8Si_5$ phase solidification in the AlCuYb [44] and AlCuGd [45] alloys. The volume fraction of the high Mn and Si-rich phases is very low (some peaks marked in the XRD patterns in Figure 2c,d). Magnesium in the investigated alloys led to the Mg_2Si phase (black particles in Figure 2a,b) solidification. The as-cast composition of the Al solid solution is presented in Table 2.

Table 2. As-cast composition of the Al solid solution.

Alloy	Al	Cu	Mg	Yb or Gd	Zr	Mn
AlCuYbMg	bal.	1.3–1.4	0.6–0.8	0.1–0.3	0.3–0.5	0.6–0.8
AlCuGdMg	bal.	1.2–1.4	0.8–0.9	0.1–0.3	0.4	0.6–0.8

DSC curves of the AlCuYbMg and AlCuGdMg alloys are presented in Figure 3. The solidus temperatures of the Mg-free AlCuYbZrMn and AlCuGdZrMn alloys are 607 and 615 °C, respectively [24]. Formation of the Mg_2Si phase in the investigated AlCuYbMg and AlCuGdMg alloys provides a decrease in the solidus temperature to 568 (Figure 3a) and 575 °C (Figure 3b), respectively.

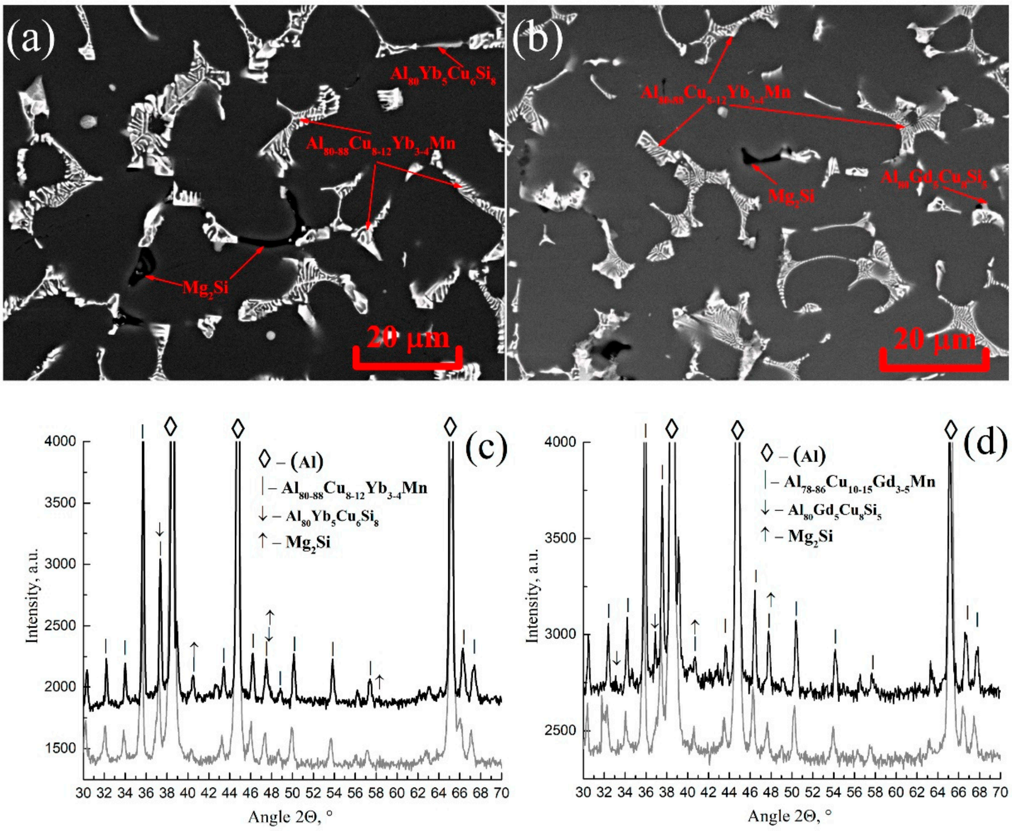

Figure 2. As-cast microstructure and phase composition of the (**a**,**c**) AlCuYbMg and (**b**,**d**) AlCuGdMg alloys ((**a**,**b**)—SEM-BSE phase composition, (**c**,**d**)—XRD (grey lines—Mg-,Si- and Fe-free alloys)).

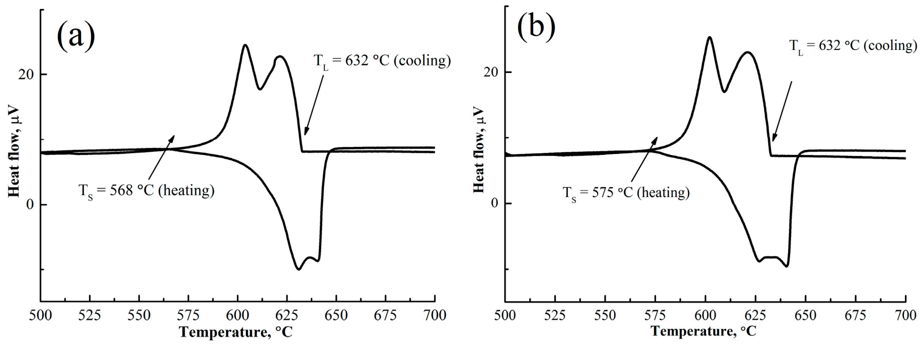

Figure 3. DSC curves of the (**a**) AlCuYbMg and (**b**) AlCuGdMg alloys.

The solution treatment temperatures of 555 and 565 °C for the AlCuYbMg and AlCuGdMg alloys, respectively, were chosen in accordance with the measured solidus temperature. The microstructures of the AlCuYbMg and AlCuGdMg alloys after 3 h of solution treatment are presented in Figure 4. The intermetallic phase particles fragmentized, spheroidized and grew to 1–3 μm. The non-equilibrium part of the intermetallic phases dissolved and provided an increase in the Cu and Mg content in the Al solid solution (compare the Tables 2 and 3). Fine white particles are clearly seen in the Al solid solution in SEM (Figure 4). A parallel process with solution treatment is the decomposition of the supersaturated Al solid solution by Zr, Mn and Yb or Gd.

Figure 5 demonstrates the TEM microstructures of the AlCuYbMg and AlCuGdMg alloys after 3 h of solution treatment at 555 °C and 565 °C, and quenching and aging at 210 °C for 3 h. The $L1_2$-Al_3(Zr,Yb) or $L1_2$-Al_3(Zr,Gd) and $Al_{20}Cu_2Mn_3$ phase precipitates were nucleated during solution treatment. Typical spherical precipitates with a coherent boundary with the Al solid solution (insert in Figure 4a) are homogenously distributed in the microstructure (Figure 5). The average sizes of the L1$_2$-Al$_3$(Zr,Yb) and L1$_2$-Al$_3$(Zr,Gd) precipitates are 28 ± 6 nm and 32 ± 4 nm, respectively (Figure 4). For comparison, the precipitates sizes in the AlCuYbZrMn and AlCuGdZrMn alloys after solution treatment at 590 and 605 °C are 38 ± 10 nm and 45 ± 16 nm [19]. Al$_{20}$Cu$_2$Mn$_3$ phase precipitates formed with a finer size of 100–200 nm in comparison with the same particles in the Mg-free alloys [24].

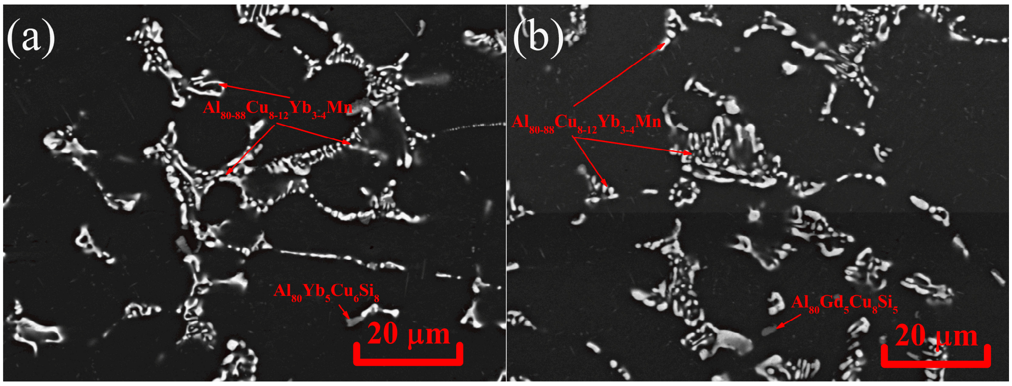

Figure 4. Microstructures of the (**a**) AlCuYbMg and (**b**) AlCuGdMg alloys after 3 h of solution treatment at (**a**) 555 °C and (**b**) 565 °C (SEM-BSE).

Table 3. Composition of the Al solid solution after 3 h of solution treatment.

Alloy	Al	Cu	Mg	Yb or Gd	Zr	Mn
AlCuYbMg	bal.	2.5–2.6	1.0–1.1	0.1–0.3	0.3–0.5	0.6–0.8
AlCuGdMg	bal.	2.0–2.2	1.1–1.2	0.1–0.3	0.4	0.6–0.8

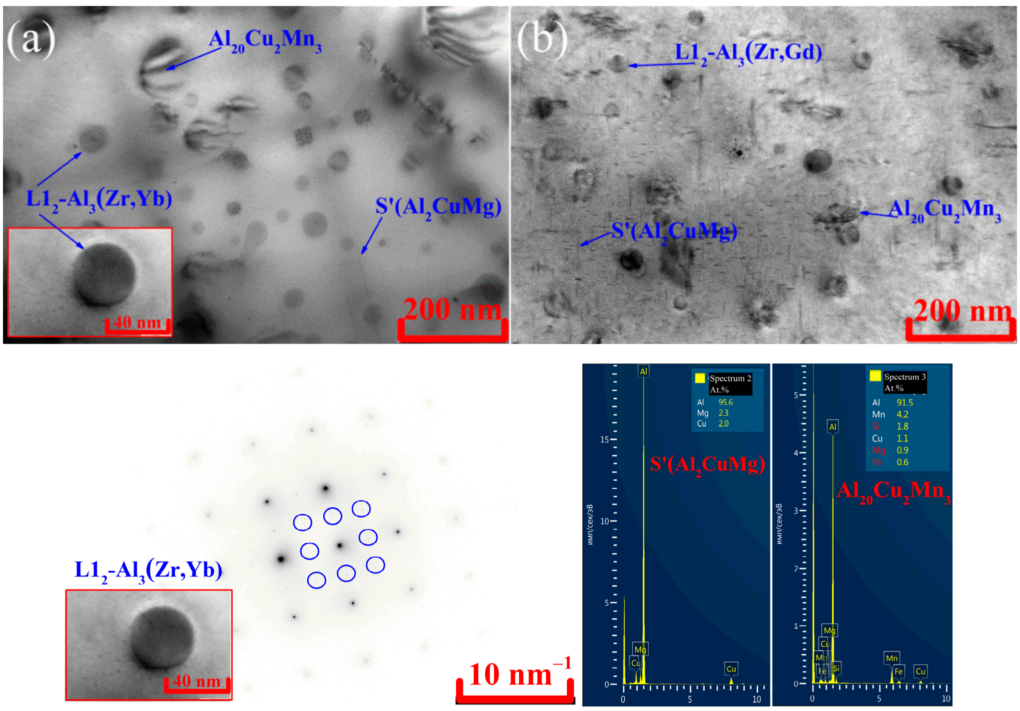

Figure 5. Microstructures of the (**a**) AlCuYbMg and (**b**) AlCuGdMg alloys after 3 h of solution treatment at (**a**) 555 °C and (**b**) 565 °C, quenching and aging at 210 °C for 3 h, and FFT pattern of L1$_2$-Al$_3$(Zr,Yb), and EDX spectrum from S′ and Al$_{20}$Cu$_2$Mn$_3$ phases (TEM).

AlCuYbMg and AlCuGdMg alloys were aged at 150, 180 and 210 °C after 3 h of solution treatment and quenching. HV vs. time dependences are presented in Figure 6. After being supersaturated by Cu and Mg, and after quenching, the Al solid solution decomposed with S′(Al_2CuMg) precipitates nucleation. The highest hardening effect was achieved after 3 h of aging at 210 °C in both alloys due to S′(Al_2CuMg) precipitates. Typical disk-shaped precipitates are identified in the TEM images in Figure 5.

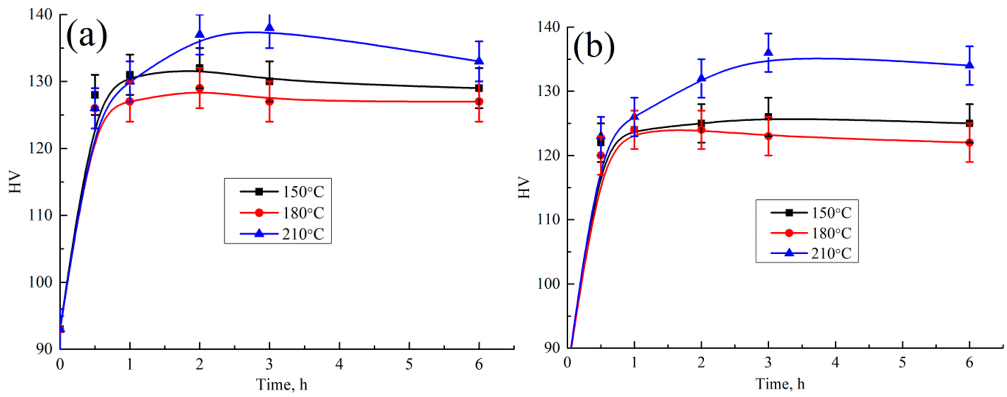

Figure 6. Aging curves of the (**a**) AlCuYbMg and (**b**) AlCuGdMg alloys.

Table 4 and Figure 7 demonstrate the results of the tensile test and typical tensile curves at different temperatures of quenching and aging at 210 °C for 3 h alloys. The UTS of the AlCuYbMg and AlCuGdMg alloys at room temperature are 338 and 299 MPa, respectively. For comparison, commercial Al-5Cu-0.8Mn alloys have the same UTS of 313–334 MPa [2]. However, the casting properties of the novel alloys are better. The HCI of the AlCuYbMg and AlCuGdMg alloys is 12–14 mm but for commercial Al-5Cu-0.8Mn alloys it is closer to 16 mm [2–5]. The UTS decreases to 219–270 MPa with an increase in the temperature of the tensile test to 200–250 °C. At the same time the elongation significantly increases. The rupture stress at 250 °C for 100 h under stress is 111–113 MPa. For comparison, the rupture stress at 260 °C for 100 h under stress is 95 MPa for a commercial 201.0 Al alloy [2]. Novel AlCuYbMg and AlCuGdMg alloys are a potential option for castings for high temperature application.

Table 4. Tensile test results at indicated temperature.

Alloy	20 °C			200 °C			250 °C		
	YS, MPa	UTS, MPa	El., %	YS, MPa	UTS, MPa	El., %	YS, MPa	UTS, MPa	El., %
AlCuYbMg	312 ± 3	338 ± 1	0.6 ± 0.1	258 ± 10	270 ± 2	0.4 ± 0.2	206 ± 6	219 ± 6	1.4 ± 0.1
AlCuGdMg	298 ± 4	299 ± 4	0.2 ± 0.1	228 ± 10	234 ± 11	0.4 ± 0.1	235 ± 10	270 ± 5	4.7 ± 0.2

The yield strength (YS) of polycrystalline material is related to the critically resolved shear stress (CRSS) of the grains and the grain boundary strengthening [46–51]. In the present model, we consider five strengthening mechanisms that affect the CRSS of grains using a linear superposition:

$$\sigma_y = \Delta\sigma_{gb} + \Delta\sigma_d + \Delta\sigma_{ss} + \Delta\sigma_{ppt} + \Delta\sigma_p \quad (1)$$

where $\Delta\sigma_{gb}$ and $\Delta\sigma_d$ are the contribution from the grain boundaries and dislocations, respectively; $\Delta\sigma_{ss}$ is the contribution from the solid solution; $\Delta\sigma_{ppt}$ is the contribution from precipitates; $\Delta\sigma_p$ is the contribution from eutectic particles.

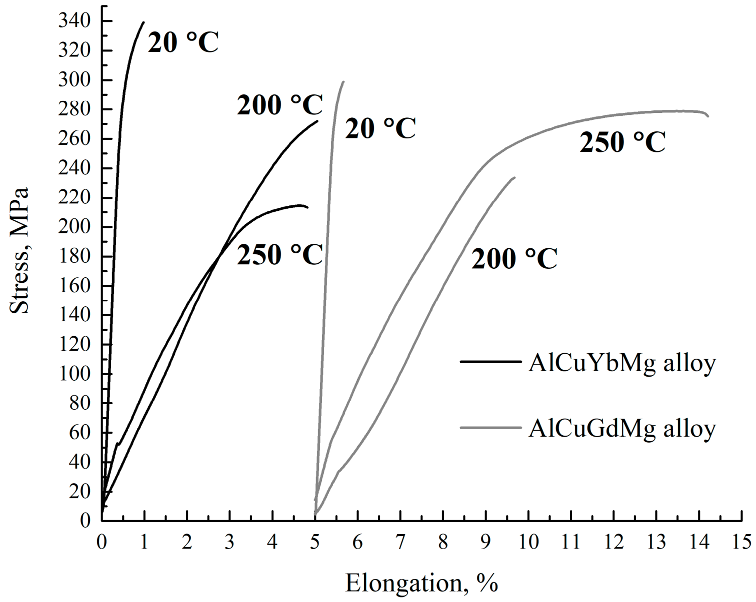

Figure 7. Typical tensile curves of the AlCuYbMg and AlCuGdMg alloys at different temperatures.

The contributions from different structure parts are summarized in Table 5. The volume fraction of the precipitates was calculated from the Al-Zr, Al-Yb, Al-Gd, Al-Cu-Mg and Al-Cu-Mg-Mn phase diagrams. The main strengthening effects of 54–60 MPa and 138–153 MPa were achieved from $L1_2$ and S′ precipitates, respectively. The calculated σ_y values are consistent with the experimental value of YS (Table 4).

Table 5. Calculated contribution from different structure parts.

Equation	Structure Parameters	AlCuYbMg	AlCuGdMg
$\Delta\sigma_{gb} = \sigma_0 + kd^{-0.5}$ [34–36]	$\sigma_0 = 10$ MPa, $k = 0.065$ MPa/m^{-2}	18.4	16.5
$\Delta\sigma_d = M\alpha_1 Gb\sqrt{\rho_{dis}}$ [34]	ρ_{dis}= 109 sm^{-2} [2]	21.2	21.2
$\Delta\sigma_{ss}$= 13.8C_{Cu}+18.6C_{Mg} [46]	C_{Cu} = 0.12%, C_{Mg} = 0.1%	3.5	3.5
$\Delta\sigma_p$ (Orovan equation [46])	r = 750 nm, f = 0.08	8.6	8.6
$\Delta\sigma_{ppt}$ (Orovan equations for spherical [46] and disc shaped particles [50])	$L1_2$ (r_{Yb} = 14 nm, r_{Gd} = 16 mn, f = 0.007)	60.2	54.4
	$Al_{20}Cu_2Mn_3$ (r = 150 nm, f_{Yb} = 0.0054, f_{Gd} = 0.004)	14	12
	S′(Al_2CuMg) (d_{Yb} = 200 nm, d_{Gd} = 100 nm, h = 1.5 nm, f_{Yb} = 0.04, f_{Gd} = 0.037	153.9	138.6
σ_y, MPa		279.8	254.8

4. Conclusions

1. Ytterbium in combination with Zr and Ti provide greater refining than gadolinium. The average grains of the AlCuYbMg and AlCuGdMg alloys are 60 ± 12 and 100 ± 15 μm, respectively.
2. $Al_{80\text{-}88}Cu_{8\text{-}12}Yb_{3\text{-}4}Mn$ and $Al_{78\text{-}86}Cu_{10\text{-}15}Gd_{3\text{-}5}Mn$ phases of the solidification origin form in the investigated AlCuYbMg and AlCuGdMg alloys. In addition, Mn-rich phase particles with about 10%Mn were identified in the AlCuYbMg alloy. The formula of this phase can be written as $Al_{22}Cu_3Mn_2Yb$. Magnesium led to the Mg_2Si phase solidification.
3. The $L1_2$-Al_3(Zr,Yb) or $L1_2$-Al_3(Zr,Gd) and $Al_{20}Cu_2Mn_3$ phase precipitates were nucleated during solution treatment. The average sizes of the $L1_2$-Al_3(Zr,Yb) and $L1_2$-

$Al_3(Zr,Gd)$ are 28 ± 6 nm and 32 ± 4 nm, respectively. $Al_{20}Cu_2Mn_3$ phase precipitates formed with a finer size 100–200 nm.

4. The highest hardening effect was achieved after 3 h of aging at 210 °C in both alloys due to S′(Al_2CuMg) precipitates. Typical disk-shaped precipitates were identified in the TEM. The UTS of the AlCuYbMg and AlCuGdMg alloys at room temperature are 338 and 299 MPa, respectively. The UTS decreases to 220–272 MPa when increasing the temperature of the tensile test to 200–250 °C. At the same time the elongation significantly increases. The rupture stress at 250 °C for 100 h under stress is 111–113 MPa.
5. The contribution from different structure parts in the yield strength was calculated. The main strengthening effects of 54–60 MPa and 138–153 MPa were achieved from $L1_2$ and S′ precipitates, respectively. The calculated values of YS are consistent with the experimental data.

Author Contributions: Conceptualization, A.V.P.; methodology, O.I.M. and S.M.A.; formal analysis, O.I.M., S.M.A. and A.V.P.; investigation, O.I.M., M.V.G. and A.V.P.; data curation, S.M.A., R.Y.B. and I.S.L.; writing—original draft preparation, A.V.P.; writing—review and editing, A.V.P.; visualization, M.V.G. and A.V.P.; supervision, R.Y.B. and A.V.P.; funding acquisition, R.Y.B. All authors have read and agreed to the published version of the manuscript.

Funding: The work was supported by the Russian Science Foundation (Project No. 21-79-00193).

Conflicts of Interest: The authors declare no conflict of interest.

References

1. AIH Committee. *ASM Handbook Vol. 2: Properties and Selection—Nonferrous Alloys and Special-Purpose Materials*; ASM International: Materials Park, OH, USA, 2001; ISBN 0871700077.
2. Zolotorevsky, V.S.; Belov, N.A.; Glazoff, M.V. *Casting Aluminum Alloys*; Alcoa Technical Center: New Kensington, PA, USA, 2007; ISBN 9780080453705.
3. Eskin, D.G.; Suyitno; Katgerman, L. Mechanical properties in the semi-solid state and hot tearing of aluminium alloys. *Prog. Mater. Sci.* **2004**, *49*, 629–711. [CrossRef]
4. Zolotorevskii, V.S.; Pozdnyakov, A.V.; Churyumov, A.Y. Search for promising compositions for developing new multiphase casting alloys based on Al-Cu-Mg matrix using thermodynamic calculations and mathematic simulation. *Phys. Met. Metallogr.* **2012**, *113*, 1052–1060. [CrossRef]
5. Pozdniakov, A.V.; Zolotorevskiy, V.S. Determining hot cracking index of Al–Si–Cu–Mg casting alloys calculated using effective solidification range. *Int. J. Cast Met. Res.* **2014**, *27*, 193–198. [CrossRef]
6. Li, M.; Wang, H.; Wei, Z.; Zhu, Z. The effect of Y on the hot-tearing resistance of Al–5wt.% Cu based alloy. *Mater. Des.* **2010**, *31*, 2483–2487. [CrossRef]
7. Krachan, T.; Stel'makhovych, B.; Kuz'ma, Y. The Y–Cu–Al system. *J. All. Comp.* **2003**, *349*, 134–139. [CrossRef]
8. Zhang, L.; Masset, P.J.; Tao, X.; Huanga, G.; Luo, H.; Liu, L.; Jin, Z. Thermodynamic description of the Al–Cu–Y ternary system. *CALPHAD Comput. Coupling Phase Diagr. Thermochem.* **2011**, *35*, 574–579. [CrossRef]
9. Zhang, L.G.; Liu, L.B.; Huang, G.X.; Qi, H.Y.; Jia, B.R.; Jin, Z.P. Thermodynamic assessment of the Al–Cu–Er system. *CALPHAD Comput. Coupling Phase Diagr. Thermochem.* **2008**, *32*, 527–534. [CrossRef]
10. Zhang, L.; Masset, P.J.; Cao, F.; Meng, F.; Liu, L.; Jin, Z. Phase relationships in the Al-rich region of the Al–Cu–Er system. *J. All. Comp.* **2011**, *509*, 3822–3831. [CrossRef]
11. Huang, G.; Liu, L.; Zhang, L.; Jin, Z. Thermodynamic description of the al-cu-yb ternary system supported by first-principles calculations. *J. Min. Metall. Sect. B Metall.* **2016**, *52*, 177–183. [CrossRef]
12. Belov, N.A.; Khvan, A.V.; Alabin, A.N. Microstructure and phase composition of Al-Ce-Cu alloys in the Al-rich corner. *Mater. Sci. Forum* **2006**, *519*, 395–400. [CrossRef]
13. Belov, N.A.; Khvan, A.V. The ternary Al-Ce-Cu phase diagram in the aluminum-rich corner. *Acta Mater.* **2007**, *55*, 5473–5482. [CrossRef]
14. Pozdniakov, A.V.; Barkov, R.Y. Microstructure and materials characterisation of the novel Al–Cu–Y alloy. *Mater. Sci. Technol.* **2018**, *34*, 1489–1496. [CrossRef]
15. Pozdnyakov, A.V.; Barkov, R.Y.; Sarsenbaev, Z.; Amer, S.M.; Prosviryakov, A.S. Evolution of Microstructure and Mechanical Properties of a New Al–Cu–Er Wrought Alloy. *Phys. Met. Metallogr.* **2019**, *120*, 614–619. [CrossRef]
16. Amer, S.M.; Barkov, R.Y.; Yakovtseva, O.A.; Pozdniakov, A.V. Comparative Analysis of Structure and Properties of Quasibinary Al–6.5Cu–2.3Y and Al–6Cu–4.05Er Alloys. *Phys. Met. Metallogr.* **2020**, *121*, 476–482. [CrossRef]
17. Amer, S.; Barkov, R.; Pozdniakov, A. Microstructure and mechanical properties of novel quasibinary al-cu-yb and al-cu-gd alloys. *Metals* **2021**, *11*, 476. [CrossRef]

18. Amer, S.M.; Barkov, R.Y.; Yakovtseva, O.A.; Loginova, I.S.; Pozdniakov, A.V. Effect of Zr on microstructure and mechanical properties of the Al–Cu–Er alloy. *Mater. Sci. Technol.* **2020**, *36*, 453–459. [CrossRef]
19. Pozdniakov, A.V.; Barkov, R.Y.; Amer, S.M.; Levchenko, V.S.; Kotov, A.D.; Mikhaylovskaya, A.V. Microstructure, mechanical properties and superplasticity of the Al–Cu–Y–Zr alloy. *Mater. Sci. Eng. A* **2019**, *758*, 28–35. [CrossRef]
20. Amer, S.M.; Mikhaylovskaya, A.V.; Barkov, R.Y.; Kotov, A.D.; Mochugovskiy, A.G.; Yakovtseva, O.A.; Glavatskikh, M.V.; Loginova, I.S.; Medvedeva, S.V.; Pozdniakov, A.V. Effect of Homogenization Treatment Regime on Microstructure, Recrystallization Behavior, Mechanical Properties, and Superplasticity of Al-Cu-Er-Zr Alloy. *JOM* **2021**, *73*, 3092–3101. [CrossRef]
21. Mamzurina, O.I.; Amer, S.M.; Loginova, I.S.; Glavatskikh, M.V.; Mochugovskiy, A.G.; Barkov, R.Y.; Pozdniakov, A.V. Effect of Zr on Microstructure and Mechanical Properties of the Al–Cu–Yb and Al–Cu–Gd Alloys. *Metals* **2022**, *12*, 479. [CrossRef]
22. Amer, S.M.; Barkov, R.Y.; Pozdniakov, A.V. Effect of Mn on the Phase Composition and Properties of Al–Cu–Y–Zr Alloy. *Phys. Met. Metallogr.* **2020**, *121*, 1227–1232. [CrossRef]
23. Amer, S.; Yakovtseva, O.; Loginova, I.; Medvedeva, S.; Prosviryakov, A.; Bazlov, A.; Barkov, R.; Pozdniakov, A. The Phase Composition and Mechanical Properties of the Novel Precipitation-Strengthening Al-Cu-Er-Mn-Zr Alloy. *Appl. Sci.* **2020**, *10*, 5345. [CrossRef]
24. Amer, S.M.; Mamzurina, O.I.; Loginova, I.S.; Glavatskikh, M.V.; Barkov, R.Y.; Pozdniakov, A.V. Effect of Mn Addition on the Phase Composition and Strengthening Behavior of AlCuYbZr and AlCuGdZr Alloys. *JOM* **2022**, *74*, 3646–3654. [CrossRef]
25. Amer, S.M.; Barkov, R.Y.; Prosviryakov, A.S.; Pozdniakov, A.V. Structure and Properties of New Heat-Resistant Cast Alloys Based on the Al–Cu–Y and Al–Cu–Er Systems. *Phys. Met. Metallogr.* **2021**, *122*, 908–914. [CrossRef]
26. Amer, S.M.; Barkov, R.Y.; Prosviryakov, A.S.; Pozdniakov, A.V. Structure and Properties of New Wrought Al–Cu–Y- and Al–Cu–Er-Based Alloys. *Phys. Met. Metallogr.* **2021**, *122*, 915–922. [CrossRef]
27. Xiao, D.; Huang, B. Effect of Yb addition on precipitation and microstructure of Al-Cu-Mg-Ag alloys. *Trans. Nonferrous Met. Soc.* **2007**, *17*, 1181–1185. [CrossRef]
28. Chen, K.H.; Fang, H.C.; Zhang, Z.l.; Chen, X.; Liu, G. Effect of of Yb, Cr and Zr additions on recrystallization and corrosion resistance of Al–Zn–Mg–Cu alloys Author links open overlay panel. *Mater. Sci. Eng. A* **2008**, *497*, 426–431. [CrossRef]
29. Fang, H.C.; Luo, F.H.; Chen, K.H. Effect of intermetallic phases and recrystallization on the corrosion and fracture behavior of an Al-Zn-Mg-Cu-Zr-Yb-Cr alloy. *Mater. Sci. Eng. A* **2017**, *648*, 480–490. [CrossRef]
30. Fang, H.C.; Chen, K.H.; Chen, X.; Chao, H.; Peng, G.S. Effect of Cr, Yb and Zr additions on localized corrosion of Al–Zn–Mg–Cu alloy. *Cor. Sci.* **2009**, *51*, 2872–2877. [CrossRef]
31. Zhang, X.G.; Mei, F.Q.; Zhang, H.Y.; Wang, S.H.; Fang, C.F.; Hao, H. Effects of Gd and Y additions on microstructure and properties of Al–Zn–Mg–Cu–Zr alloys. *Mater. Sci. Eng. A* **2012**, *552*, 230–235. [CrossRef]
32. Peng, G.; Chen, K.; Fang, H.; Chen, S. Effect of Cr and Yb additions on microstructure and properties of low copper Al–Zn–Mg–Cu–Zr alloy. *Mater. Des.* **2012**, *36*, 279–283. [CrossRef]
33. Li, J.H.; Suetsugu, S.; Tsunekawa, Y.; Schumacher, P. Refinement of Eutectic Si Phase in Al-5Si Alloys with Yb Additions. *Metall. Mater. Trans. A.* **2013**, *44*, 669–681. [CrossRef]
34. Jia, K.; Yu, W.-B.; Yao, J.-M.; Zhang, S.; Wu, H. Al–9.00%Si–0.25%Mg alloys modified by ytterbium. *Rare Met.* **2017**, *36*, 95–100. [CrossRef]
35. Zhiming, S.H.I.; Qiang, W.A.N.G.; Yuting, S.H.I.; Ge, Z.H.A.O.; Zhang, R. Microstructure and mechanical properties of Gd-modified A356 aluminum alloys. *J. Rare Earths* **2015**, *33*, 1004–1009. [CrossRef]
36. Peng, G.; Chen, K.; Fang, H.; Chen, S. A study of nanoscale Al_3(Zr,Yb) dispersoids structure and thermal stability in Al–Zr–Yb alloy. *Mater. Sci. Eng. A* **2012**, *535*, 311–315. [CrossRef]
37. Zhang, Y.; Zhou, W.; Gao, H.; Han, Y.; Wang, K.; Wang, J.; Sun, B.; Gu, S.; You, W. Precipitation evolution of Al–Zr–Yb alloys during isochronal aging. *Scr. Mater.* **2013**, *69*, 477–480. [CrossRef]
38. Wen, S.P.; Gao, K.Y.; Huang, H.; Wang, W.; Nie, Z.R. Role of Yb and Si on the precipitation hardening and recrystallization of dilute Al–Zr alloys. *J. Alloy. Compd.* **2014**, *599*, 65–70. [CrossRef]
39. Cacciamani, G.; De Negri, S.; Saccone, A.; Ferro, R. The Al–R–Mg (R=Gd, Dy, Ho) systems. Part I: Experimental investigation. *Intermetallics* **2003**, *11*, 1125–1134. [CrossRef]
40. Van Dalen, M.E.; Dunand, D.C.; Seidman, D.N. Microstructural evolution and creep properties of precipitation-strengthened Al–0.06Sc–0.02Gd and Al–0.06Sc–0.02Yb (at.%) alloys. *Acta Mater.* **2011**, *59*, 5224–5237. [CrossRef]
41. Hao, H.L.; Ni, D.R.; Zhang, Z.; Wang, D.; Xiao, B.L.; Ma, Z.Y. Microstructure and mechanical properties of Al-Mg-Er sheets jointed by friction stir welding. *Mater. Des.* **2013**, *52*, 706–712. [CrossRef]
42. Yang, D.; Li, X.; He, D.; Huang, H. Effect of minor Er and Zr on microstructure and mechanical properties of Al-Mg-Mn alloy (5083) welded joints. *Mater. Sci. Eng. A* **2013**, *561*, 226–231. [CrossRef]
43. Pozdniakov, A.V.; Yarasu, V.; Barkov, R.Y.; Yakovtseva, O.A.; Makhov, S.V.; Napalkov, V.I. Microstructure and mechanical properties of novel Al-Mg-Mn-Zr-Sc-Er alloy. *Mater. Lett.* **2017**, *202*, 116–119. [CrossRef]
44. Barkov, M.V.; Mamzurina, O.I.; Glavatskikh, M.V.; Barkov, R.Y.; Pozdniakov, A.V. Structure and Properties of Al–Cu–Yb Alloy with Iron and Silicon Impurities. *Russ. J. Non-Ferrous Met.* **2022**, *63*, 434–440. [CrossRef]
45. Barkov, M.V.; Mamzurina, O.I.; Glavatskikh, M.V.; Barkov, R.Y.; Pozdniakov, A.V. The Effects of Impurities on the Phase Composition and the Properties of the Al–Cu–Gd Alloy. *Phys. Met. Metallogr.* **2022**, *123*, 604–608. [CrossRef]

46. Starink, M.J.; Wang, S.C. A model for the yield strength of overaged Al–Zn–Mg–Cu alloys. *Acta Mater.* **2003**, *51*, 5131–5150. [CrossRef]
47. Deschamps, A.; Brechet, Y. Influence of predeformation and ageing of an Al–Zn–Mg alloy—II. Modeling of precipitation kinetics and yield stress. *Acta Mater.* **1998**, *47*, 293–305. [CrossRef]
48. Ma, K.; Wen, H.; Hu, T.; Topping, T.D.; Isheim, D.; Seidman, D.N.; Lavernia, E.J.; Schoenung, J.M. Mechanical behavior and strengthening mechanisms in ultrafine grain precipitation-strengthened aluminum alloy. *Acta Mater.* **2014**, *62*, 141–155. [CrossRef]
49. Dong, J.; Gao, N.; Chen, Y.; Cao, L.; Song, H.; Fröck, H.; Milkereit, B.; Starink, M.J. Achieving ultra-high strength of Al-Cu-Li alloys by the combination of high pressure torsion and age-hardening. *Mater. Sci. Eng. A* **2022**, *832*, 142504. [CrossRef]
50. Chen, Y.; Gao, N.; Sha, G.; Ringer, S.P.; Starink, M.J. Microstructural evolution, strengthening and thermal stability of an ultrafine-grained Al–Cu–Mg alloy. *Acta Mater.* **2016**, *109*, 202–212. [CrossRef]
51. Weakley-Bollin, S.C.; Donlon, W.; Donlon, W.; Wolverton, C.; Allison, J.E.; Jones, J.W. Modeling the age-hardening behavior of Al-Si-Cu alloys. *Metall. Mater. Trans. A* **2004**, *35*, 2407–2418. [CrossRef]